J Mater Sci: Mater Electron (2015) 26:8774–8783
DOI 10.1007/s10854-015-3557-3

# Facile electrospinning construction and characteristics of coaxial nanobelts with simultaneously tunable magnetism and color-tuned photoluminescence bifunctionality

**Hongjin Xue[1] · Xiaopeng Sun[1] · Jingwei Bi[1] · Tianyang Wang[1] · Ji Han[1] · Qianli Ma[1] · Lei Han[1] · Xiangting Dong[1]**

Received: 24 June 2015 / Accepted: 27 July 2015 / Published online: 2 August 2015


**Abstract** New-typed coaxial nanobelts with magnetism and tunable fluorescent color bifunctionality have been successfully fabricated by electrospinning technology using a specially designed coaxial-spinneret. The synthesized coaxial nanobelts are composed of $CoFe_2O_4$/polymethyl methacrylate (PMMA) as the magnetic core and [$Tb(BA)_3$(phen) + $Eu(BA)_3$(phen)]/PMMA (BA = benzoic acid, phen = 1,10-phenanthroline) as the photoluminescent shell. The morphology and properties of the final products have been investigated in detail by X-ray diffractometry, scanning electron microscopy, biological microscopy, vibrating sample magnetometry and fluorescence spectroscopy. The emitting color of the coaxial nanobelts can be tuned by adjusting the mass ratios of $Tb(BA)_3$(phen) and $Eu(BA)_3$(phen) in a wide color range from red to yellow to green under the excitation of 274-nm single-wavelength ultraviolet light. The luminescent intensity and magnetic property of the coaxial nanobelts can also be tuned. Furthermore, the coaxial nanobelts provide higher luminescent performance than $CoFe_2O_4$/[$Tb(BA)_3$(phen) + $Eu(BA)_3$(phen)]/PMMA composite nanobelts. This new type of magnetic and color-tunable bifunctional coaxial nanobelt has the potential to be applied in novel nano-biolabel materials, drug delivery materials, and future nanodevices owing to their excellent magnetic-fluorescent properties, flexibility, and insolubility.

✉ Xiangting Dong
dongxiangting888@163.com

[1] Key Laboratory of Applied Chemistry and Nanotechnology at Universities of Jilin Province, Changchun University of Science and Technology, Changchun 130022, China

## 1 Introduction

Recently, electrospinning, which has been recognized as one of the most convenient, direct and economical methods for the fabrication of polymer nanofibers, arouses much attention of materials scientists all over the world [1–5]. This method not only attracts extensive academic investigations, but is also applied in many areas such as filtration [6], optical and chemical sensors [7], biological scaffolds [8], display devices [9] and nanocables [10, 11].

In recent years, the development of the magnetic-luminescent bifunctional nanomaterials has attracted particular interest because of their wide applications in biological systems such as diagnostic analysis and controlled drug release [12–18]. The current studies on magnetic-luminescent bifunctional nanomaterials are mainly focused on nanoparticles [19, 20]. To obtain magnetic-fluorescent nanomaterials with new morphology, the fabrication of one-dimensional magnetic-fluorescent nanomaterials is a meaningful and urgent subject of study. As a commonly used magnetic material, cobalt ferrite ($CoFe_2O_4$) has received considerable attention owing to its moderate saturation magnetization, high coercivity and excellent physical and chemical stability, as well as its potential applications in electronic devices, drug delivery technology, magnetic resonance imaging, and information storage [21, 22]. Presently, some multicolored and color-tunable luminescent materials have been prepared by introducing two or more different luminescent materials [23–26]. Among various luminescent materials, Tb(III) and Eu(III) complexes have excellent luminescent properties owing to the f–f electron transition of $Tb^{3+}$ ions and $Eu^{3+}$ ions, and they have received a widespread attention due to their excellent performance. Armelao et al. [27] anchored Eu(III) and Tb(III) complexes onto a single $SiO_2$

transparent layer by sol–gel dip-coating under acidic conditions. This allows high loading of tailored proportions of the red and green emitters within the films and results in highly uniform and easily color-tunable luminescent layers. Lai et al. [28] synthesized color-tunable luminescent materials based on α, ω-diethyl malonate terminated polydimethylsiloxane (EP) and lanthanide ions. The obtained materials exhibited excellent narrow-width red (or green) emissions when incorporating $Eu^{3+}$ (or $Tb^{3+}$) ions into EP. Moreover, the luminescence spectra of the EP heterometallic complexes were changed via tuning the ratios of $Eu^{3+}$ and $Tb^{3+}$ ions, yielding a wide range of colors.

Nanobelt is a kind of nanomaterial with a special morphology [29–31]. It has attracted increasing interest from scientists owing to its anisotropy, large width-thickness ratio, and unique optical, electrical, and magnetic properties. We have attempted to assemble $CoFe_2O_4$ nanofibers and $Tb(BA)_3(phen) + Eu(BA)_3(phen)$ complexes into polymethyl methacrylate (PMMA) based nanobelts. However, the obtained $CoFe_2O_4$/[$Tb(BA)_3(phen) + Eu(BA)_3(phen)$]/PMMA composite nanobelts suffer a heavy loss of fluorescence intensity. To ultimately reduce the impact of $CoFe_2O_4$ nanofibers on the fluorescent property, in this study, we designed coaxial nanobelts with a new nanostructure via electrospinning technology using a specially designed coaxial-spinneret. Of the coaxial nanobelt, the core is composed of template PMMA containing $CoFe_2O_4$ nanofibers, and the shell consists of PMMA containing $Tb(BA)_3(phen)$ and $Eu(BA)_3(phen)$ complexes. This new nanostructure can successfully help to realize the assembling magnetism and tunable color bifunction into one strip of [$CoFe_2O_4$/PMMA]@[[$Tb(BA)_3(phen) + Eu(BA)_3(phen)$]/PMMA] coaxial nanobelt and the effective separation of $CoFe_2O_4$ from the rare earth luminescent complexes. It is expected that this novel morphology will lead to bifunctional flexible nanobelts with excellent magnetism and luminescence being obtained. To the best of our knowledge, these new structured flexible magnetic and color-tunable bifunctional coaxial nanobelts prepared by means of one-step electrospinning have not been reported in any literature. The structure, fluorescence, and magnetism of the coaxial nanobelts were systematically studied, and some new results were obtained.

## 2 Experimental sections

### 2.1 Materials

Methylmethacrylate (MMA), Polyvinyl pyrrolidone (PVP, $Mw = 1{,}300{,}000$), benzoylperoxide (BPO), $Tb_4O_7$, $Eu_2O_3$, benzoic acid (BA), phenanthroline (phen), $Fe(NO_3)_3$, $Co(NO_3)_2$, nitric acid, $CHCl_3$, DMF, and deionized water were used. All the reagents were of analytical grade. The purity of $Tb_4O_7$ and $Eu_2O_3$ was 99.99 %. The deionized water was homemade.

### 2.2 Preparation of $CoFe_2O_4$ nanofibers via electrospinning technology

A traditional single-spinneret electrospinning instrument was used to prepare $CoFe_2O_4$ nanofibers. The spinning solution for preparing $CoFe_2O_4$ nanofibers was prepared as follows: 2.1767 g of $Fe(NO_3)_3$, 0.8232 g of $Co(NO_3)_2$ and 3.9000 g of PVP were dissolved in 23.1000 g of DMF with continuous stirring. The spinning solution was stirred for 12 h to form homogeneous mixture solutions for next-step electrospinning. Then, the spinning solutions was injected into a traditional single-spinneret electrospinning setup, [$Fe(NO_3)_3 + Co(NO_3)_2$]/PVP composite nanofibers were prepared by electrospinning. The electrospinning parameters were as follows: the distance between the spinneret (a plastic nozzle) and collector was fixed at 18–20 cm and high voltage power supply was maintained at 12–15 kV. The room temperature was 20–24 °C and the relative humidity was 60–70 %. $CoFe_2O_4$ nanofibers could be obtained when the relevant composite nanofibers were annealed in air at 900 °C for 6 h with a heating rate of 1 °C $min^{-1}$.

### 2.3 Synthesis of $Tb(BA)_3(phen)$ and $Eu(BA)_3(phen)$ complexes

$Tb(BA)_3(phen)$ complexes were synthesized according to the traditional method as described in the literatures [32]. 1.8690 g of $Tb_4O_7$ was dissolved in 20 mL of concentrated nitric acid at 120 °C. Then $Tb(NO_3)_3{\cdot}6H_2O$ powders were acquired by evaporation of excess nitric acid and water by heating. $Tb(NO_3)_3$ ethanol solution was prepared by adding 20 mL of anhydrous ethanol into the above $Tb(NO_3)_3{\cdot}6H_2O$. 3.6638 g BA and 1.9822 g of phen were dissolved in 200 mL of ethanol. $Tb(NO_3)_3$ solution was then added into the mixture solution of BA and phen under magnetic stirring at 60 °C for 3 h. The precipitates were collected by filtration and dried at 60 °C for 12 h. The synthetic method of $Eu(BA)_3(phen)$ complexes was similar to the above method, except that the using dosages of $Eu_2O_3$, BA and phen were 1.7600, 3.6640 and 1.9822 g, respectively.

### 2.4 Preparation of PMMA

PMMA used in this study was prepared by oxidative polymerization of MMA [33]. MMA (100 mL) and BPO (0.1000 g) were mixed in a 250-mL three-necked flask with a backflow device and stirred vigorously at 90–95 °C. When the viscosity of the solution reached a certain value just like that of glycerol, the heating was stopped and it was

**Table 1** Composition of the spinning solutions I

| Spinning solutions I | $CoFe_2O_4$ nanofibers/g | PMMA/g | DMF/g | $CHCl_3$/g |
|---|---|---|---|---|
| I-1 | 0.6500 | 1.3000 | 0.9091 | 9.0909 |
| I-2 | 1.3000 | 1.3000 | 0.9091 | 9.0909 |
| I-3 | 2.6000 | 1.3000 | 0.9091 | 9.0909 |

**Table 2** Composition of the spinning solutions II

| Spinning solutions II | $Tb(BA)_3(phen)$:$Eu(BA)_3(phen)$ (mass ratio) | $Tb(BA)_3(phen)$/g | $Eu(BA)_3(phen)$/g | PMMA/g | DMF/g | $CHCl_3$/g |
|---|---|---|---|---|---|---|
| II-1 | 10:0 | 0.1950 | 0 | 1.3000 | 0.9091 | 9.0909 |
| II-2 | 7:3 | 0.1365 | 0.0585 | 1.3000 | 0.9091 | 9.0909 |
| II-3 | 5:5 | 0.0975 | 0.0975 | 1.3000 | 0.9091 | 9.0909 |
| II-4 | 3:7 | 0.0585 | 0.1365 | 1.3000 | 0.9091 | 9.0909 |
| II-5 | 1:9 | 0.0195 | 0.1755 | 1.3000 | 0.9091 | 9.0909 |
| II-6 | 0:10 | 0 | 0.1950 | 1.3000 | 0.9091 | 9.0909 |

left to naturally cool down to room temperature. The obtained gelatinous solution was then loaded into test tubes, and the influx height was 5–7 cm. After that, the tubes were put in an electric vacuum oven at 50 °C for 48 h, and the gelatinous solution was then solidified. Finally, the temperature in the oven was raised to 110 °C for 2 h to terminate the reaction.

### 2.5 Preparation of spinning solutions for fabricating magnetism and color-tunable bifunctional coaxial nanobelts

Two different kinds of spinning solution were prepared to fabricate the coaxial nanobelts. The spinning solution for the core of coaxial nanobelts was composed of $CoFe_2O_4$ nanofibers, PMMA, $CHCl_3$, and DMF (spinning solutions I, see Table 1).

Another spinning solution for the shell of the coaxial nanobelts consisted of [$Tb(BA)_3(phen)$ + $Eu(BA)_3$ (phen)], PMMA, $CHCl_3$, and DMF (spinning solutions II). To study the fluorescent performances of [$CoFe_2O_4$/PMMA]@[[$Tb(BA)_3(phen)$ + $Eu(BA)_3(phen)$]/PMMA] coaxial nanobelts, different mass ratios of $Tb(BA)_3$ (phen) to $Eu(BA)_3(phen)$ were added into spinning solutions II. The dosages of these materials were summarized in Table 2, and the spinning solutions for fabricating different [$CoFe_2O_4$/PMMA]@[[$Tb(BA)_3(phen)$ + $Eu(BA)_3(phen)$]/PMMA] coaxial nanobelts samples were listed in Table 3.

### 2.6 Electrospinning equipment for fabricating coaxial nanobelts

A schematic diagram of the equipment for the electrospinning process of coaxial nanobelts is presented in Fig. 1 (left), and an enlarged schematic diagram for the coaxial spinneret is shown in Fig. 1 (right). Spinning solution I was injected into the inner plastic syringe while spinning solution II was also loaded into the outer one. A flat iron net was put about 18 cm away from the tip of the plastic nozzle as a nanobelts collector. A positive direct current (DC) voltage of 6 kV was applied between the spinneret and the collector to generate stable, continuous PMMA-based coaxial nanobelts at 24–26 °C, and the relative humidity was 48–53 %.

**Table 3** Spinning solutions for fabricating different [$CoFe_2O_4$/PMMA]@[[$Tb(BA)_3(phen)$ + $Eu(BA)_3(phen)$]/PMMA] coaxial nanobelts samples

| Sample | Spinning solutions | |
|---|---|---|
| $S_1$ | I-1 | II-1 |
| $S_2$ | I-1 | II-2 |
| $S_3$ | I-1 | II-3 |
| $S_4$ | I-1 | II-4 |
| $S_5$ | I-1 | II-5 |
| $S_6$ | I-1 | II-6 |
| $S_7$ | I-2 | II-3 |
| $S_8$ | I-3 | II-3 |

### 2.7 Fabrication of $CoFe_2O_4$/[$Tb(BA)_3(phen)$ + $Eu(BA)_3(phen)$]/PMMA composite nanobelts

As the comparative sample, $CoFe_2O_4$/[$Tb(BA)_3(phen)$ + $Eu(BA)_3(phen)$]/PMMA composite nanobelts were fabricated by mixing spinning solution I-2 and spinning solution II-3 together at the volume ratio of 1:1 and electrospun using traditional single-spinneret electrospinning method. This fabrication of the $CoFe_2O_4$/[$Tb(BA)_3(phen)$ + $Eu(BA)_3(phen)$]/

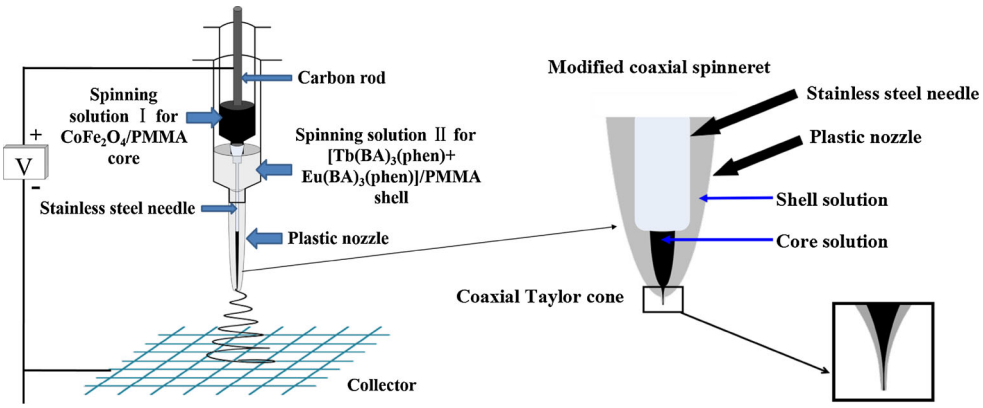


**Fig. 1** Schematic diagram of the equipment for the electrospinning process of coaxial nanobelts

PMMA composite nanobelt is an easy way for obtaining the magnetic-fluorescent bifunctional nanomaterial: simply mix the $CoFe_2O_4$ nanofibers, rare complexes and PMMA together to form nanobelts. A syringe containing a plastic nozzle was used as the spinneret, and the other spinning parameters were the same as those for fabricating [$CoFe_2O_4$/PMMA]@[[Tb(BA)$_3$(phen) + Eu(BA)$_3$(phen)]/PMMA] coaxial nanobelts.

### 2.8 Characterization methods

The as-prepared $CoFe_2O_4$ nanofibers, [$CoFe_2O_4$/PMMA]@[[Tb(BA)$_3$(phen) + Eu(BA)$_3$(phen)]/PMMA] coax-ial nanobelts and $CoFe_2O_4$/[Tb(BA)$_3$(phen) + Eu(BA)$_3$(phen)]/PMMA composite nanobelts were identified by an X-ray powder diffractometer (Bruker, D8 FOCUS) with $Cu_{K\alpha}$ radiation. The operation voltage and current were kept at 40 kV and 20 mA, respectively. The morphology and internal structure of the coaxial nanobelts was observed by a field-emission scanning electron microscope (FESEM, XL-30) and a biological microscope (CVM500E), respectively. The fluorescent properties of the samples were investigated by Hitachi fluorescence spectrophotometer F-7000. Then, the magnetic performance of samples was measured by a vibrating sample magnetometer (VSM, MPMS SQUID XL). All the measurements were performed at room temperature.

## 3 Results and discussion

### 3.1 Phase analyses

The phase compositions of the $CoFe_2O_4$ nanofibers and [$CoFe_2O_4$/PMMA]@[[Tb(BA)$_3$(phen) + Eu(BA)$_3$(phen)]/PMMA] coaxial nanobelts ($S_7$, see Table 3 in Sect. 2) were characterized by means of X-ray diffractometry (XRD) analysis, as shown in Fig. 2. The XRD patterns of the as-prepared $CoFe_2O_4$ nanofibers conform to the cubic spinel structure of $CoFe_2O_4$ (PDF 22-1086), and the XRD analysis results of the [$CoFe_2O_4$/PMMA]@[[Tb(BA)$_3$(phen) + Eu(BA)$_3$(phen)]/PMMA] coaxial nanobelts and $CoFe_2O_4$/[Tb(BA)$_3$(phen) + Eu(BA)$_3$(phen)]/PMMA composite nanobelts demonstrate that both of them contain $CoFe_2O_4$ nanofibers.

### 3.2 Morphology and internal structure

The morphology of the as-prepared $CoFe_2O_4$ nanofibers was observed by means of scanning electron microscope (SEM), as presented in Fig. 3a. The diameter distribution of the $CoFe_2O_4$ nanofibers is almost uniform, and the fiber width is determined to be 73.43 ± 8.00 nm (Fig. 3b). The morphology and structure of [$CoFe_2O_4$/PMMA]@[[Tb(BA)$_3$(phen) + Eu(BA)$_3$(phen)]/PMMA] coaxial nanobelts ($S_7$) were characterized by the combination of SEM and biological microscope (BM). As seen from Fig. 3c, the width of the coaxial nanobelt is 9.95 ± 0.36 μm (Fig. 3d) and the thickness is about 923 nm. Depending on the transmission light of the BM, the inner structure of the coaxial nanobelts can also be observed. As revealed in Fig. 3e, a clear coaxial structure can be seen in the [$CoFe_2O_4$/PMMA]@[[Tb(BA)$_3$(phen) + Eu(BA)$_3$(phen)]/PMMA] nanobelt. The core of the coaxial nanobelt is about 8 μm in width and it contains large quantities of dark-colored $CoFe_2O_4$ nanofibers, and the shell is transparent. To illustrate the advantages of the coaxial nanostructure of the magnetic-fluorescent bifunctional nanobelts, the $CoFe_2O_4$/[Tb(BA)$_3$(phen) + Eu(BA)$_3$(phen)]/PMMA composite nanobelts, as a comparative sample, were also fabricated by mixing spinning solutions I-2 and II-3 together. The BM image of the $CoFe_2O_4$/[Tb(BA)$_3$(phen) + Eu(BA)$_3$(phen)]/PMMA composite nanobelt is shown in Fig. 3f. It can be seen that the $CoFe_2O_4$ nanofibers are distributed throughout the $CoFe_2O_4$/[Tb(BA)$_3$(phen) + Eu(BA)$_3$(phen)]/PMMA composite nanobelt.

From the SEM and BM observations, we have proven that the [$CoFe_2O_4$/PMMA]@[[Tb(BA)$_3$(phen) + Eu(BA)$_3$

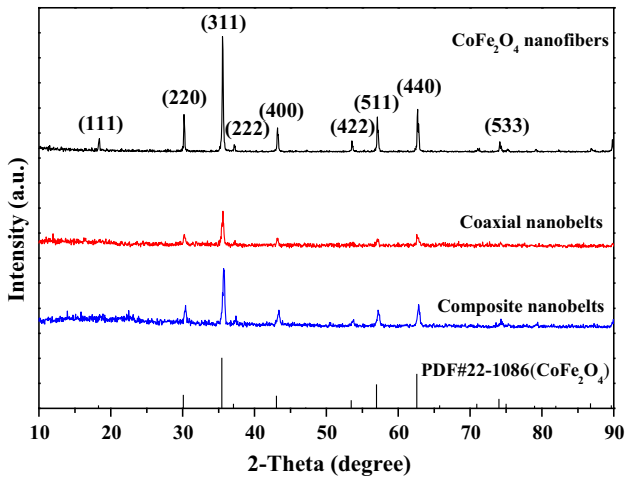


**Fig. 2** XRD patterns of $CoFe_2O_4$ nanofibers, [$CoFe_2O_4$/PMMA]@[[$Tb(BA)_3$(phen) + $Eu(BA)_3$(phen)]/PMMA] coaxial nanobelts and $CoFe_2O_4$/[$Tb(BA)_3$(phen) + $Eu(BA)_3$(phen)]/PMMA composite nanobelts

(phen)]/PMMA] coaxial nanobelts, a new and interesting nanostructure, have been successfully fabricated.

### 3.3 Fluorescence properties

We firstly investigate the luminescent characteristics of [$CoFe_2O_4$/PMMA]@[$Tb(BA)_3$(phen)/PMMA] coaxial nanobelts ($S_1$) and [$CoFe_2O_4$/PMMA]@[$Eu(BA)_3$(phen)/PMMA] coaxial nanobelts ($S_6$). The excitation and emission spectra of [$CoFe_2O_4$/PMMA]@[$Tb(BA)_3$(phen)/PMMA] coaxial nanobelts ($S_1$) are demonstrated in Fig. 4. When the monitoring wavelength is set to be 545 nm, a broad excitation band extending from 200 to 450 nm with the maximum at 274 nm can be observed, which is assigned to the $\pi \rightarrow \pi^*$ electron transition of the conjugated double bonds of the ligands. Under the excitation of 274-nm ultraviolet light, characteristic emission peaks of $Tb^{3+}$ ions are observed, which are ascribed to the energy levels transitions of $^5D_4 \rightarrow {}^7F_6$ (490 nm), $^5D_4 \rightarrow {}^7F_5$ (545 nm), $^5D_4 \rightarrow {}^7F_4$ (585 nm), $^5D_4 \rightarrow {}^7F_3$ (622 nm), and the $^5D_4 \rightarrow {}^7F_5$ and $^5D_4 \rightarrow {}^7F_6$ hypersensitive transitions at 545 and 490 nm are the predominant emission peaks.

The excitation and emission spectra of [$CoFe_2O_4$/PMMA]@[$Eu(BA)_3$(phen)/PMMA] coaxial nanobelts ($S_6$) are indicated in Fig. 5. When the monitoring wavelength is 616 nm, a broad excitation band (left) extending from 200 to 450 nm with the maximum at 274 nm is observed, which is assigned to the $\pi \rightarrow \pi^*$ electron transition of the conjugated double bonds of the ligands. The right side in the figure is the emission spectrum of the sample. It is found that under the excitation of 274-nm ultraviolet light, the sample exhibits red emissions of predominant peaks at 593 nm and 616 nm attributed to the $^5D_0 \rightarrow {}^7F_1$ and $^5D_0 \rightarrow {}^7F_2$ energy levels transitions of $Eu^{3+}$ ions, respectively. Furthermore, one can see that both the [$CoFe_2O_4$/PMMA]@[$Tb(BA)_3$(phen)/PMMA] coaxial nanobelts and [$CoFe_2O_4$/PMMA]@[$Eu(BA)_3$(phen)/PMMA] coaxial nanobelts can be most effectively excited using 274-nm single-wavelength ultraviolet light.

The emission spectra of [$CoFe_2O_4$/PMMA]@[[$Tb(BA)_3$(phen) + $Eu(BA)_3$(phen)]/PMMA] coaxial nanobelts with different mass ratios of $Tb(BA)_3$(phen) to $Eu(BA)_3$(phen) under the excitation of 274-nm ultraviolet light are indicated in Fig. 6. The cores of these coaxial nanobelts were fabricated using spinning solution I-1 (see Table 1 in Sect. 2), and the mass ratios of $Tb(BA)_3$(phen) to $Eu(BA)_3$(phen) (the shells of these coaxial nanobelts) are 10:0 ($S_1$), 7:3 ($S_2$), 5:5 ($S_3$), 3:7 ($S_4$), 1:9 ($S_5$) and 0:10 ($S_6$), respectively. One can see that with the increase of the mass ratio of $Tb(BA)_3$(phen) to $Eu(BA)_3$(phen), the green fluorescence emissions at 490 and 545 nm enhance gradually, while the orange and red fluorescence emissions at 593 and 616 nm gradually decrease. Therefore, it is evidently found that the emission spectra of [$CoFe_2O_4$/PMMA]@[[$Tb(BA)_3$(phen) + $Eu(BA)_3$(phen)]/PMMA] coaxial nanobelts could be tuned by adjusting the mass ratio of $Tb(BA)_3$(phen) and $Eu(BA)_3$(phen) complexes in the coaxial nanobelts.

Generally, color can be represented by the Commission Internationale de L'Eclairage (CIE) 1931 chromaticity coordinates. Figure 7 reveals the CIE coordinate diagram of [$CoFe_2O_4$/PMMA]@[[$Tb(BA)_3$(phen) + $Eu(BA)_3$(phen)]/PMMA] coaxial nanobelts under the excitation of 274-nm ultraviolet light. It is found that the emitting color of samples could be tuned by adjusting the mass ratio of $Tb(BA)_3$(phen) and $Eu(BA)_3$(phen) complexes in a wide color range of green–yellow–red under the excitation of 274-nm single-wavelength ultraviolet light.

Meanwhile, the fluorescence emission spectra (excited by 274-nm ultraviolet light) of [$CoFe_2O_4$/PMMA]@[[$Tb(BA)_3$(phen) + $Eu(BA)_3$(phen)]/PMMA] coaxial nanobelts containing different amounts of $CoFe_2O_4$ nanofibers are indicated in Fig. 8a. The mass ratios of $CoFe_2O_4$ to PMMA are 1:2 ($S_3$),1:1 ($S_7$) and 2:1($S_8$), respectively. The shells of these coaxial nanobelts were fabricated using spinning solution II-3 (see Table 2 in Sect. 2). From comparing emission spectra A to D in Fig. 8a, it is found that the emission intensity of the [$CoFe_2O_4$/PMMA]@[[$Tb(BA)_3$(phen) + $Eu(BA)_3$(phen)]/PMMA] coaxial nanobelts is decreased with increasing in the amount of $CoFe_2O_4$ nanofibers introduced into the cores of the coaxial nanobelts. This phenomenon can be explained as the light absorption of $CoFe_2O_4$ nanofibers [34]. From the UV–Vis diffuse reflectance spectrum of $CoFe_2O_4$ nanofibers illustrated in Fig. 8b, it is seen that the $CoFe_2O_4$ nanofibers can absorb visible light (400-700 nm) and much more easily absorb the

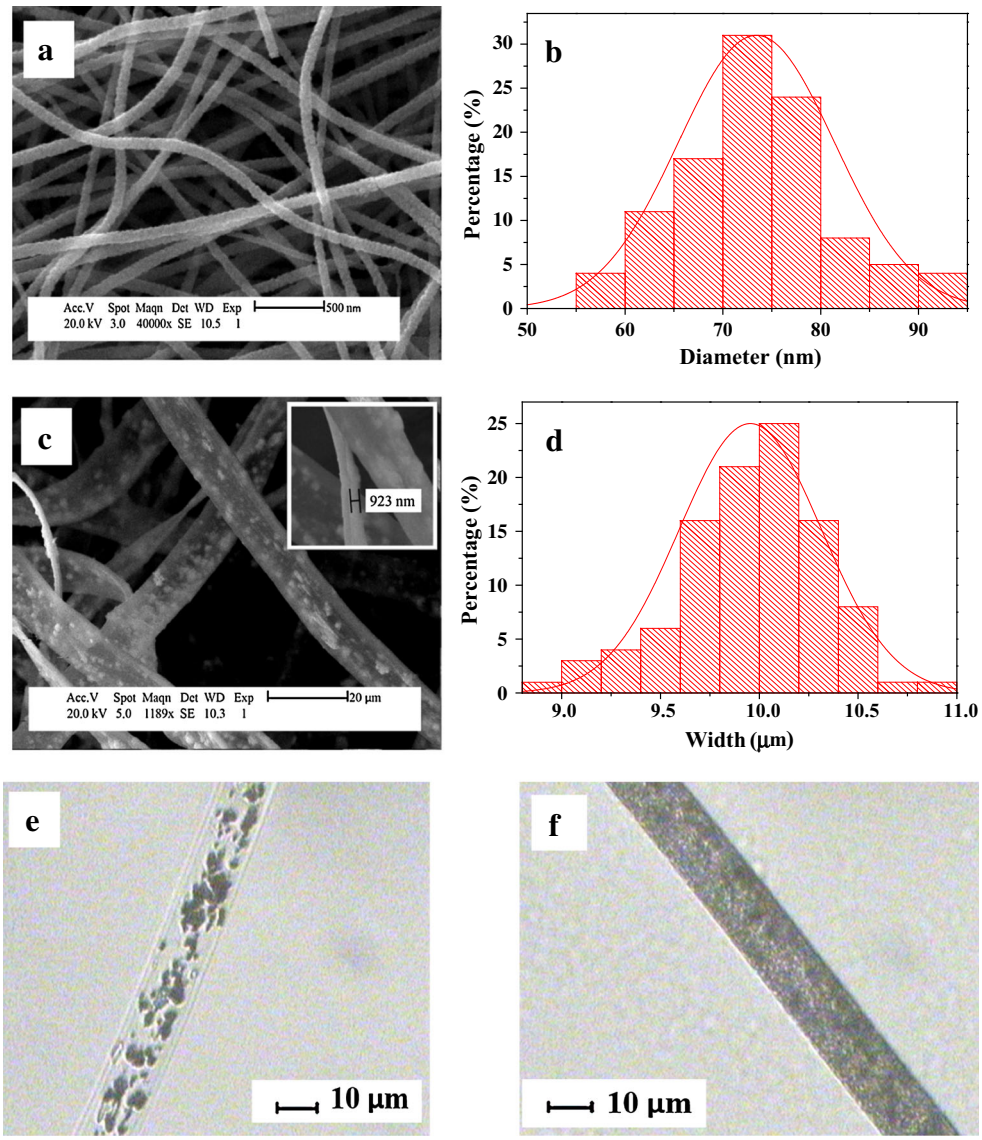


**Fig. 3** SEM image (**a**) and histogram (**b**) of diameter distribution of $CoFe_2O_4$ nanofibers; SEM (**c**) image and histogram (**d**) of width distribution of [$CoFe_2O_4$/PMMA]@[[$Tb(BA)_3$(phen) + $Eu(BA)_3$(phen)]/PMMA] coaxial nanobelts; and BM images of [$CoFe_2O_4$/PMMA]@[[$Tb(BA)_3$(phen) + $Eu(BA)_3$(phen)]/PMMA] coaxial nanobelts (**e**) and $CoFe_2O_4$/[$Tb(BA)_3$(phen) + $Eu(BA)_3$(phen)]/PMMA composite nanobelts (**f**)

ultraviolet light (<400 nm). Thus, the exciting light and emitting light are absorbed by the $CoFe_2O_4$ nanofibers and the intensities are decreased. Furthermore, the light absorption would become stronger with introduction of more $CoFe_2O_4$ nanofibers into the core.

To further discuss the trend, the intensities of every emission peak of each sample versus different samples were plotted in the inset in Fig. 8a. The decreased rate of each emission peak intensity value decreases with the increase of the amount of $CoFe_2O_4$ nanofibers introduced into the core. This finding may be because the blackness of the core gradually approaches saturation, and the light absorption of the core is nearly maximized with more $CoFe_2O_4$ nanofibers introduced into the coaxial nanobelts. From the comparison between sample B and D in Fig. 8a, it is found that the emission intensity of the $CoFe_2O_4$/[$Tb(BA)_3$(phen) + $Eu(BA)_3$(phen)]/PMMA composite nanobelts is much weaker than that of the coaxial nanobelts. This heavy loss in fluorescent emission intensity is from the strong light absorption of the dark-colored $CoFe_2O_4$ nanofibers when $CoFe_2O_4$ nanofibers and [$Tb(BA)_3$(phen) + $Eu(BA)_3$(phen)] are directly blended together. As illustrated in Fig. 9, because the $CoFe_2O_4$ nanofibers are distributed over the whole parts of the $CoFe_2O_4$/[$Tb(BA)_3$(phen) +

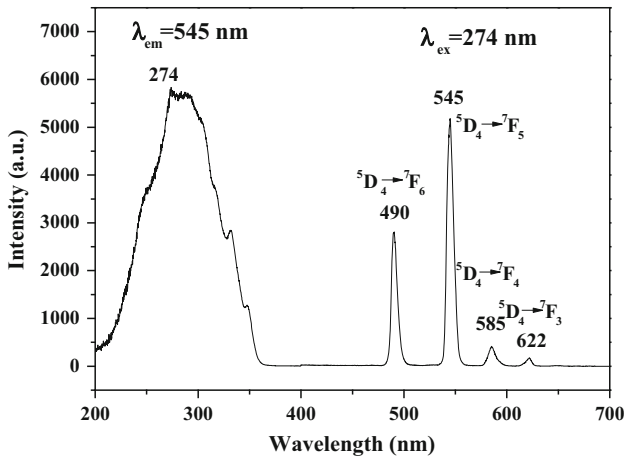


**Fig. 4** Excitation (*left*) and emission (*right*) spectra of [$CoFe_2O_4$/PMMA]@[$Tb(BA)_3$(phen)/PMMA] coaxial nanobelts ($S_1$)

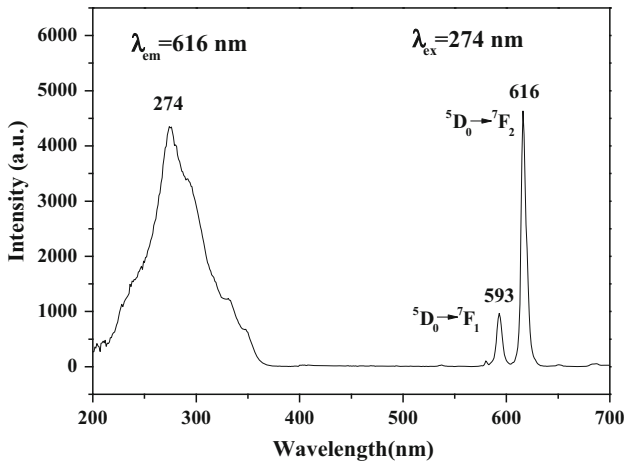


**Fig. 5** Excitation (*left*) and emission (*right*) spectra of [$CoFe_2O_4$/PMMA]@[$Eu(BA)_3$(phen)/PMMA] coaxial nanobelts ($S_6$)

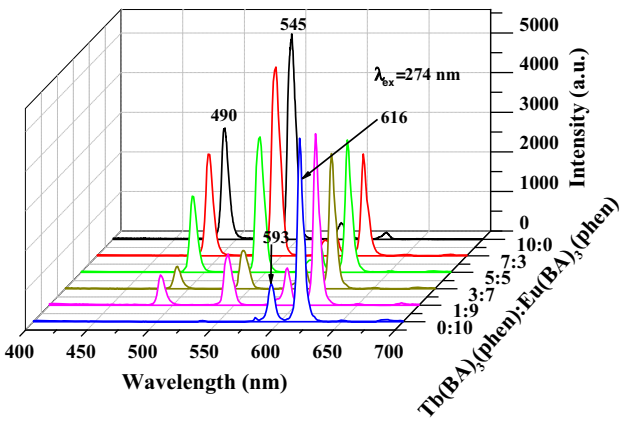


**Fig. 6** Emission spectra of [$CoFe_2O_4$/PMMA]@[[$Tb(BA)_3$(phen) + $Eu(BA)_3$(phen)]/PMMA] coaxial nanobelts with different mass ratios of $Tb(BA)_3$(phen) to $Eu(BA)_3$(phen) under the excitation of 274-nm single-wavelength ultraviolet light

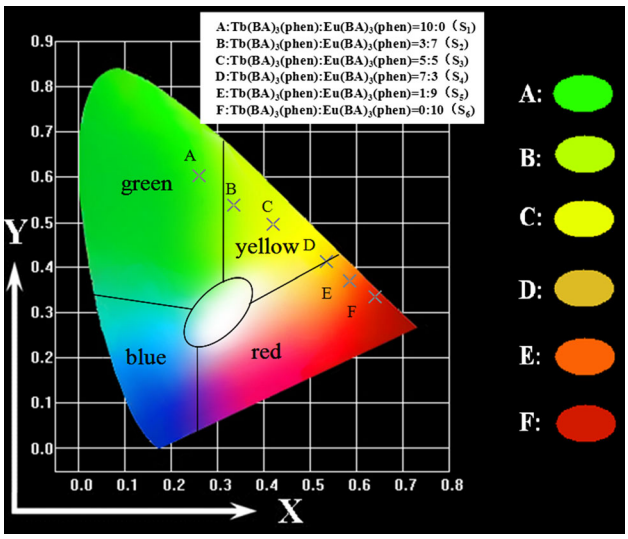


**Fig. 7** CIE chromaticity coordinates diagram of [$CoFe_2O_4$/PMMA]@[[$Tb(BA)_3$(phen) + $Eu(BA)_3$(phen)]/PMMA] coaxial nanobelts with different mass ratios of $Tb(BA)_3$(phen) to $Eu(BA)_3$(phen)

$Eu(BA)_3$(phen)]/PMMA composite nanobelts, the exciting light has to pass through many $CoFe_2O_4$ nanofibers to reach the [$Tb(BA)_3$(phen) + $Eu(BA)_3$(phen)] complexes. In this process, a large part of the exciting light has been absorbed by the $CoFe_2O_4$ nanofibers, and thus the exciting light is much weakened before it reaches the [$Tb(BA)_3$(phen) + $Eu(BA)_3$(phen)] complexes. Similarly, the light emitted by the [$Tb(BA)_3$(phen) + $Eu(BA)_3$(phen)] complexes also has to pass through the $CoFe_2O_4$ nanofibers and is absorbed by them, which results in the emitting light being severely weakened. For the [$CoFe_2O_4$/PMMA]@[[$Tb(BA)_3$(phen) + $Eu(BA)_3$(phen)]/PMMA] coaxial nanobelts, the $CoFe_2O_4$ nanofibers and [$Tb(BA)_3$(phen) + $Eu(BA)_3$(phen)] complexes are separated in their own domains of the coaxial nanobelts, so that the exciting light and emitting light in the [$Tb(BA)_3$(phen) + $Eu(BA)_3$(phen)]/PMMA domain will almost be unaffected by the $CoFe_2O_4$ nanofibers. The overall result is that the coaxial nanobelts possess a much higher fluorescent performance than the $CoFe_2O_4$/[$Tb(BA)_3$(phen) + $Eu(BA)_3$(phen)]/PMMA composite nanobelts. Thus, a stronger fluorescent emission intensity of the magnetic and color-tunable bifunctional coaxial nanobelt is achieved through isolating [$Tb(BA)_3$(phen) + $Eu(BA)_3$(phen)] from $CoFe_2O_4$ nanofibers, and the academic ideas described in the Introduction are realized.

Figure 10 is the CIE coordinate diagram of [$CoFe_2O_4$/PMMA]@[[$Tb(BA)_3$(phen) + $Eu(BA)_3$(phen)]/PMMA] coaxial nanobelts containing different amounts of $CoFe_2O_4$ nanofibers under the excitation of 274-nm ultraviolet light. It demonstrates that the emitting color of the [$CoFe_2O_4$/PMMA]@[[$Tb(BA)_3$(phen) + $Eu(BA)_3$(phen)]/PMMA]

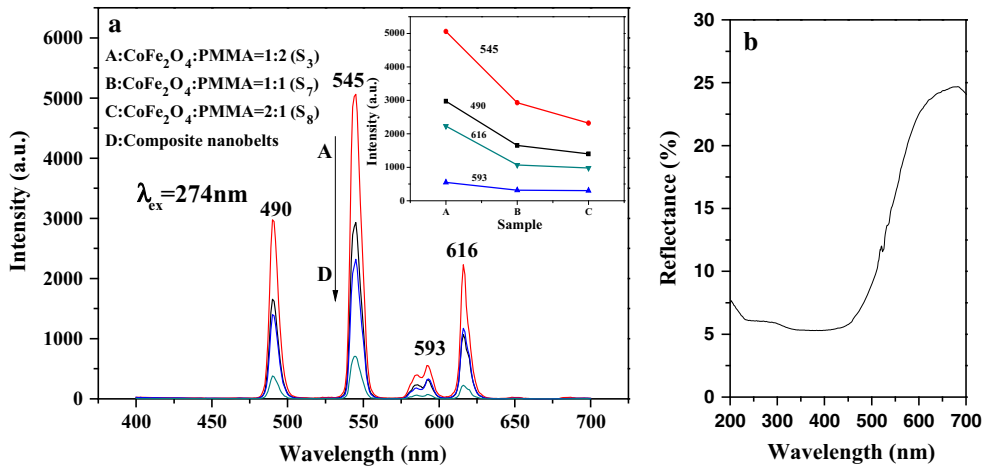


**Fig. 8** Comparison of emission spectra (**a**) of $[CoFe_2O_4/PMMA]$@ $[[Tb(BA)_3(phen) + Eu(BA)_3(phen)]/PMMA]$ coaxial nanobelts (containing different mass ratios of $CoFe_2O_4$ nanofibers), $CoFe_2O_4$/$[Tb(BA)_3(phen) + Eu(BA)_3(phen)]/PMMA$ composite nanobelts and UV–Vis diffuse reflectance spectrum (**b**) of $CoFe_2O_4$ nanofibers

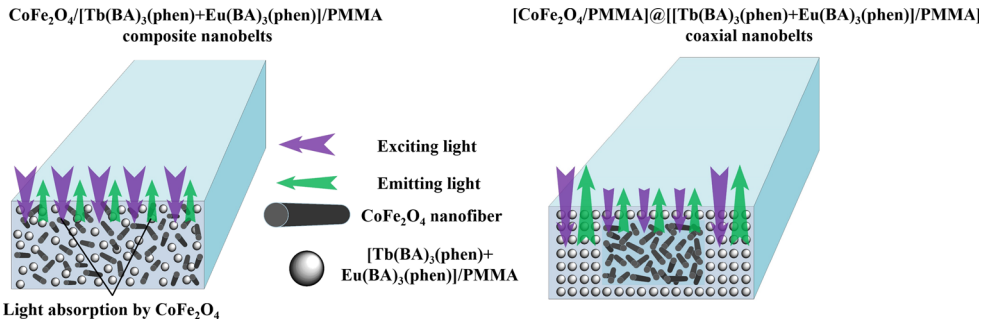


**Fig. 9** Schematic diagrams of the situation of the exciting light and emitting light in the $[CoFe_2O_4/PMMA]$@$[[Tb(BA)_3(phen) + Eu(BA)_3(phen)]/PMMA]$ coaxial nanobelts and $CoFe_2O_4/[Tb(BA)_3(phen) + Eu(BA)_3(phen)]/PMMA$ composite nanobelts

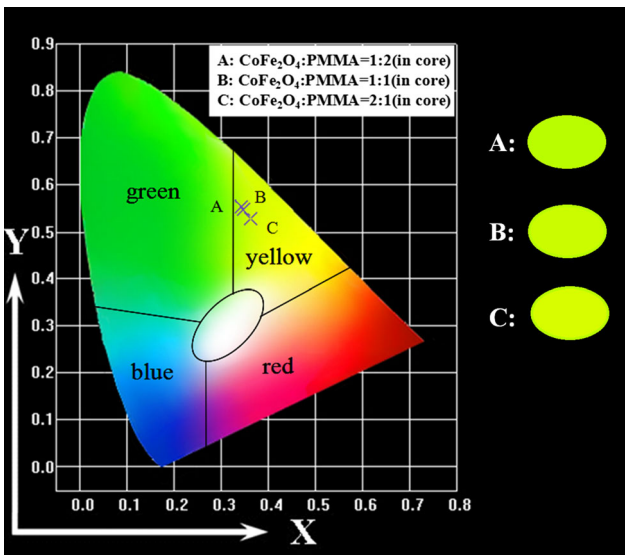


**Fig. 10** CIE chromaticity coordinates diagram of $[CoFe_2O_4/PMMA]$ @$[[Tb(BA)_3(phen) + Eu(BA)_3(phen)]/PMMA]$ coaxial nanobelts containing different mass ratios of $CoFe_2O_4$ nanofibers

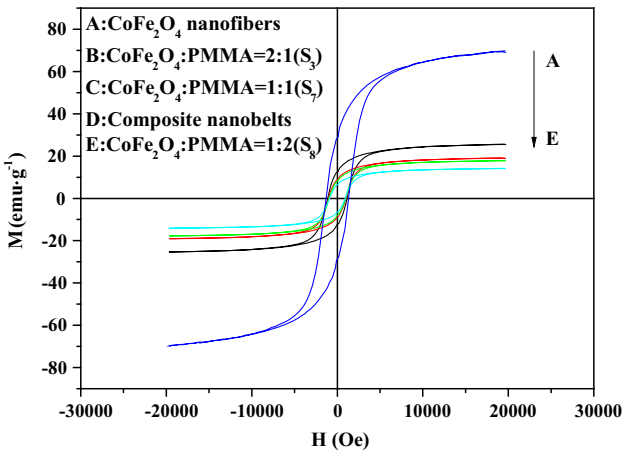


**Fig. 11** Hysteresis loops of the $CoFe_2O_4$ nanofibers, $[CoFe_2O_4/PMMA]$ @$[[Tb(BA)_3(phen) + Eu(BA)_3(phen)]/PMMA]$ coaxial nanobelts containing different mass ratios of $CoFe_2O_4$ nanofibers, and $CoFe_2O_4/[Tb(BA)_3(phen) + Eu(BA)_3(phen)]/PMMA$ composite nanobelts

**Table 4** Saturation magnetization (*Ms*), remanence ($M_r$) and coercivity (*Hc*) of samples

| Samples | $M_s$/emu $g^{-1}$ | $M_r$/emu $g^{-1}$ | $H_c$/Oe |
|---|---|---|---|
| $CoFe_2O_4$ nanofibers | 69.45 | 28.89 | 1341.41 |
| Coaxial nanobelts, $CoFe_2O_4$/PMMA = 2:1 (in core) | 25.52 | 12.61 | 1128.29 |
| Coaxial nanobelts, $CoFe_2O_4$/PMMA = 1:1 (in core) | 19.00 | 8.87 | 1065.61 |
| Coaxial nanobelts, $CoFe_2O_4$/PMMA = 1:2 (in core) | 14.17 | 6.55 | 952.78 |
| Composite nanobelts | 17.81 | 8.26 | 1015.46 |

coaxial nanobelts becomes more yellow with introducing more $CoFe_2O_4$ nanofibers, due to the stronger absorption of green light than red light by $CoFe_2O_4$, as seen in Fig. 8b.

### 3.4 Magnetic properties

The typical hysteresis loops for $CoFe_2O_4$ nanofibers, [$CoFe_2O_4$/PMMA]@[[$Tb(BA)_3$(phen) + $Eu(BA)_3$(phen)]/PMMA] coaxial nanobelts containing different mass ratios of $CoFe_2O_4$ nanofibers, and $CoFe_2O_4$/[$Tb(BA)_3$(phen) + $Eu(BA)_3$(phen)]/PMMA composite nanobelts are shown in Fig. 11, and the saturation magnetization, remanence and coercivity of the samples are listed in Table 4. It is well known that the saturation magnetization of a magnetic composite material depends on the mass percentage of the magnetic substance in the magnetic composite material [35]. It is found that saturation magnetization of [$CoFe_2O_4$/PMMA]@[[$Tb(BA)_3$(phen) + $Eu(BA)_3$(phen)]/PMMA] coaxial nanobelts is increased with the increase of the amount of $CoFe_2O_4$ nanofibers introduced into the core. The saturation magnetization of the [$CoFe_2O_4$/PMMA]@[[$Tb(BA)_3$(phen) + $Eu(BA)_3$(phen)]/PMMA] coaxial nanobelts is 8.87 emu $g^{-1}$, which is very close to of that of the $CoFe_2O_4$/[$Tb(BA)_3$(phen) + $Eu(BA)_3$(phen)]/PMMA composite nanobelts marked D (8.26 emu $g^{-1}$) in Fig. 11 because they are both prepared by spinning solution I-2 and II-3. By combining the analyses of magnetism and fluorescence, it can be found that [$CoFe_2O_4$/PMMA]@[[$Tb(BA)_3$(phen) + $Eu(BA)_3$(phen)]/PMMA] coaxial nanobelts have similar magnetic property compared to $CoFe_2O_4$/[$Tb(BA)_3$(phen) + $Eu(BA)_3$(phen)]/PMMA composite nanobelts, but the fluorescent intensity of the coaxial nanobelts is very much higher than that of the composite nanobelts. This further demonstrates that the coaxial nanobelts have better magnetic-fluorescent performance than the composite nanobelts.

## 4 Conclusions

In summary, novel flexible magnetic and color-tunable bifunctional [$CoFe_2O_4$/PMMA]@[[$Tb(BA)_3$(phen) + $Eu(BA)_3$(phen)]/PMMA] coaxial nanobelts have been successfully synthesized by electrospinning technology. The width of the coaxial nanobelts is 9.95 ± 0.36 μm and the thickness is less than 1 μm. The core of the coaxial nanobelts is composed of $CoFe_2O_4$ nanofibers and PMMA, and the shell consists of [$Tb(BA)_3$(phen) + $Eu(BA)_3$(phen)] complexes and PMMA. It is very gratifying to see that the coaxial nanobelts simultaneously possess high fluorescent intensity, tunable colors and saturation magnetization. Under the excitation of 274-nm single-wavelength ultraviolet light, the emitting color of the coaxial nanobelts can be tuned in a wide color range of red-yellow-green by adjusting the mass ratio of terbium complexes and europium complexes. Compared with the simply mixed $CoFe_2O_4$/[$Tb(BA)_3$(phen) + $Eu(BA)_3$(phen)]/PMMA composite nanobelt, which suffers a heavy loss in fluorescent emission intensity owing to the existence of the $CoFe_2O_4$ nanofibers dispersed everywhere, the impact of $CoFe_2O_4$ on the fluorescent emission intensity is significantly decreased in the coaxial nanobelts. Furthermore, the color, fluorescent intensity, and magnetism of the coaxial nanobelts can be tuned by adjusting the diversity and the mass ratios of fluorescent compounds and the amount of magnetic compound. In addition, other multifunctional nanomaterials such as tunable color-electricity or tunable color-magnetism-electricity trifunctional nanostructures can be designed and fabricated based on this novel design conception and construction technology.

**Acknowledgments** This work was financially supported by the National Natural Science Foundation of China (NSFC 50972020, 51072026), Specialized Research Fund for the Doctoral Program of Higher Education (20102216110002, 20112216120003), the Science and Technology Development Planning Project of Jilin Province (Grant Nos. 20130101001JC, 20070402).

## References

1. C. Yang, L. Hu, H.Y. Zhu, Y. Ling, J.H. Tao, C.X. Xu, J. Mater. Chem. B **3**, 2651–2659 (2015)
2. C. Azra, D. Alhazov, E. Zussman, Polymer **58**, 162–169 (2014)
3. M.R. Badrossamay, K. Balachandran, A.K. Capulli, H.M. Golecki, A. Agarwal, J.A. Goss, H. Kim, K. Shin, K.K. Parker, Biomaterials **35**, 3188–3197 (2014)
4. X.L. Hu, S. Liu, G.Y. Zhou, Y.B. Huang, Z.G. Xie, X.B. Jing, J. Controlled Release **185**, 12–21 (2014)
5. Z.Y. Zhang, C.L. Shao, X.H. Li, Y.Y. Sun, M.Y. Zhang, J.B. Mu, P. Zhang, Z.C. Guo, Y.C. Liu, Nanoscale **5**, 606–618 (2013)

6. S. Kaur, S. Sundarrajan, D. Rana, R. Sridhar, R. Gopal, T. Matsuura, S. Ramakrishna, J. Mater. Sci. **49**, 6143–6159 (2014)
7. C. Wolf, M. Tscherner, S. Köstler, Sens. Actuators B **209**, 1064–1069 (2015)
8. J. Wang, A.S. Nain, Langmuir **30**, 13641–13649 (2014)
9. B. Sun, Y.Z. Long, Z.J. Chen, S.L. Liu, H.D. Zhang, J.C. Zhang, W.P. Han, J. Mater. Chem. C **2**, 1209–1219 (2014)
10. G. Panthi, M. Park, H.Y. Kim, S.Y. Leea, S.J. Parka, J. Ind. Eng. Chem. **21**, 26–35 (2015)
11. Z. Li, H. Huang, C. Wang, Macromol. Rapid Commun. **27**, 152–155 (2006)
12. W.S. Yu, Q.L. Ma, X.L. Li, X.T. Dong, J.X. Wang, G.X. Liu, Mater. Lett. **120**, 126–129 (2014)
13. F. Bi, X.J. Dong, J.X. Wang, G.X. Liu, RSC Adv. **5**, 12571–12577 (2015)
14. S. Chidambaram, K. Baskaran, S.J. Samuel, B. Pari, A.R. Sujatha, S. Muthusamy, Mater. Sci. Forum **781**, 1–16 (2014)
15. A. Szczeszak, A. Ekner-Grzyb, M. Runowski, L. Mrówczyńska, T. Grzyb, S. Lis, J. Nanopart. Res. **17**, 1–11 (2015)
16. L.P. Singh, N.P. Singh, S.K. Srivastava, Dalton Trans. **44**, 6457–6465 (2015)
17. Y.L. Liu, J.L. Zhang, G. Cheng, G.Y. Hong, J.Z. Ni, Nanotechnology **23**, 425702 (2012)
18. R.M. Guo, J.X. Wang, X.T. Dong, Q.L. Ma, W.S. Yu, C. Song, G.X. Liu, J. Mater. Sci. **49**, 5418–5426 (2014)
19. A.F. Zedan, V. Abdelsayed, M.B. Mohamed, M.S. El-Shall, J. Nanopart. Res. **15**, 1–8 (2013)
20. M. Runowski, T. Grzyb, S. Lis, J. Nanopart. Res. **14**, 1–8 (2012)
21. W. Hu, L. Zou, R. Chen, W. Xie, X.M. Chen, N. Qin, S.W. Li, G.W. Yang, T.H. Bao, Appl. Phys. Lett. **104**, 143502 (2014)
22. Y.F. Xu, Y.Q. Ma, S.T. Xu, G.H. Zheng, Z.X. Dai, J. Mater. Sci. **50**, 4486–4494 (2015)
23. F. Wang, X. Liu, Acc. Chem. Res. **47**, 1378–1385 (2015)
24. J.H. Kim, B.K. An, S.J. Yoon, S.K. Park, J.E. Kwon, C.K. Lim, S.Y. Park, Adv. Funct. Mater. **24**, 2746–2753 (2014)
25. K. Lun, Q.L. Ma, X.T. Dong, W.S. Yu, J.X. Wang, G.X. Liu, J. Mater. Sci. Mater. Electron. **25**, 5395–5402 (2014)
26. F. Wang, X. Liu, Acc. Chem. Res. **47**, 1378–1385 (2014)
27. L. Armelao, G. Bottaro, S. Quici, M. Cavazzini, M.C. Raffo, F. Barigellettic, G. Accorsi, Chem. Commun. **28**, 2911–2913 (2007)
28. Q. Lai, H. Lu, D. Wang, H. Wang, S.Y. Feng, J. Zhang, Macromol. Chem. Phys. **212**, 1435–1442 (2011)
29. Q.L. Ma, J.X. Wang, X.T. Dong, W.S. Yu, G.X. Liu, ChemPlusChem **79**, 290–297 (2014)
30. Z.Y. Peng, Y.L. Liu, K.Q. Chen, G.J. Yang, W. Chen, Chem. Eng. J. **244**, 335–342 (2014)
31. Z. Lan, J.H. Wu, S.W. Gao, J.M. Lin, M.L. Huang, X.M. Chen, Polym. Adv. Technol. **25**, 343–346 (2014)
32. S.B. Meshkova, J. Fluoresc. **10**, 333–337 (2000)
33. B. Vazquez, S. Deb, W. Bonfield, J. Mater. Sci. Mater. Med. **8**, 455–460 (1997)
34. F. Bi, X. Dong, J. Wang, G.X. Liu, J. Mater. Sci. Mater. Electron. **25**, 4259–4267 (2014)
35. Q.L. Ma, W.S. Yu, X.T. Dong, J.X. Wang, G.X. Liu, Nanoscale **6**, 2945–2952 (2014)